Light ion isotope identification in space using a pixel detector based single layer telescope

M. Kroupa, A. A. Bahadori, T. Campbell-Ricketts, S. P. George, N. Stoffle, and C. Zeitlin

Citation: Appl. Phys. Lett. **113**, 174101 (2018); doi: 10.1063/1.5052907
View online: https://doi.org/10.1063/1.5052907
View Table of Contents: http://aip.scitation.org/toc/apl/113/17
Published by the American Institute of Physics

Light ion isotope identification in space using a pixel detector based single layer telescope

M. Kroupa,[1,2,a)] A. A. Bahadori,[3] T. Campbell-Ricketts,[4,2] S. P. George,[4,2] N. Stoffle,[1,2] and C. Zeitlin[1,2]
[1]*Leidos Innovations Corporation, Houston, Texas 77258, USA*
[2]*Space Radiation Analysis Group, NASA, JSC, Houston, Texas 77058, USA*
[3]*Department of Mechanical and Nuclear Engineering, Kansas State University, Manhattan, Kansas 66506, USA*
[4]*Department of Physics, University of Houston, Houston, Texas 77204, USA*

(Received 21 August 2018; accepted 10 October 2018; published online 25 October 2018)

It is demonstrated that modern pixel detectors can be utilized as single-layer particle telescopes, offering details of a particle's stopping power evolution surpassing those provided by multi-layer, non-pixelated instruments. For particles that stop in the detector, this advantage arises from repeatably sampling the Bragg curve: we always know which part of the Bragg peak was measured. We can then create a dE/dx_1 vs dE/dx_2 plot where the stopping power at the beginning and the end of the track is compared. We are able to identify and analyze several fine-grained features on such plots, including several related to particles that stop inside the detector, termed "stopping." Using data from an instrument aboard the International Space Station, we show that different isotopes of stopping hydrogen can be identified as their stopping powers differ. Other features of the dE/dx_1 vs dE/dx_2 plot not resolvable in multi-layer particle telescopes are also exhibited, such as nuclear interactions that occur within the sensor active volume. *Published by AIP Publishing.*
https://doi.org/10.1063/1.5052907

Space radiation presents a unique radiation detection challenge, being composed of a mix of various radiation types spanning very broad ranges of kinetic energy and energy deposition per unit path length (dE/dx). Recent advances in radiation risk modeling[1,2] require ion charge (or Z - ions in the space are fully ionized) and energy spectra, resulting in demand for detectors providing a more detailed characterization than state of the art.

Newly developed radiation monitors utilizing the Timepix chip[3] permit a much more complete understanding of the space radiation environment. Integration of front-end electronics in the pixel footprint results in a compact array of more than 65 000 detectors capable of measuring energy deposition. Together with low mass and low power consumption, detectors based on this technology are well-suited for NASA's future Exploration Missions.

Significant advances have also been made in pixel detector data analysis. Specifically, particle-by-particle characterization, instead of simple rate measurements or techniques that rely on spectra processing, is possible.[4,5] Pixel data can be used to reconstruct the incident kinetic energy of heavy charged particles by segmenting particle tracks into separate spatial regions.[6] A similar method can be used to address slowing-down and stopped particles,[7] which have been shown to impact absorbed dose measurements obtained at different detector orientations.[8]

Particle telescopes are commonly used in high-energy and nuclear physics. They consist of multiple layers of detectors which are selected with respect to the quanta measured. Telescopes and conceptually related systems can range from simple configurations of multiple silicon diodes to extremely large and complex systems, such as Time Projection Chambers which have been used at large accelerators for several decades. The particle telescope approach has been successfully employed in space, where mass, volume, and power constraints typically limit the size and performance of the instruments. Examples of such instruments are numerous and include detectors aboard the Advanced Composition Explorer and Geostationary Operational Environmental Satellite spacecraft, among many others. In the context of human precursor missions to deep space, instruments include Martian Radiation Environment Experiment aboard the Mars Odyssey orbiter,[9] Mars Science Laboratory Radiation Assessment Detector on the Curiosity rover,[10] and Cosmic Ray Telescope for the Effects of Radiation on the Lunar Reconnaissance Orbiter.[11] Similar instruments are also used on the International Space Station (ISS), such as Anomalous Long Term Effects on Astronauts.[12] These telescopes, which vary in mass from less than 2 kg to 30 kg, use coincidence logic to trigger on events in which the incident particle traverses multiple detectors. By measuring the energy deposited in different layers of the telescope, more information about interacting particles can be acquired. In some designs, a calorimeter is employed to measure the energy of medium-energy particles, typically those with energies less than a few hundred mega-electron volts per nucleon, thereby allowing analysis via the ΔE-E_{tot} method.

Here, the advantages of pixel-based detectors are demonstrated for characterization of the space environment. Although the pixel detectors described here are composed of only a single active layer, segmentation of particle tracks provides multiple dE/dx samples, similar to the concept employed in earlier ground-based particle detectors.[13] These

[a)]Author to whom correspondence should be addressed: martin.kroupa@nasa.gov

pixel detectors represent a less expensive, less massive, and more compact system than possible with previous generations of multilayer charged particle telescopes.

The Timepix read-out chip consists of a 256-by-256 array of pixels, each with spectroscopic capability. The pixel pitch is 55 μm. A 500 μm-thick pixelated silicon semiconductor sensor is bump-bonded to the Timepix chip. When an ionizing particle enters the sensor, it creates electron-hole pairs, which then travel through the reverse-biased semiconductor (100 V), producing signals measured in multiple pixels. Signal amplitudes are related to energy deposition in the sensor.[14,15]

Timepix data acquisition consists of taking snapshots, known as "frames," of charged-particle tracks over an adjustable time period. Within a frame, each ionizing particle traversing the sensor creates a collection of contiguous pixels with non-zero signal, referred to as a "cluster." A cluster can be many tens of pixels in size. By analyzing the cluster, one can determine properties of the particle that produced the track, including incident angle and path length through the sensor. Coupled with accurate energy calibration, a high-fidelity measurement of dE/dx results.[5,7,16]

Clusters can be separated into multiple segments or sub-clusters.[6] While this methodology in general allows for very fine segmentation, in this application, we create two sub-clusters, permitting two-dimensional plots of dE/dx_1 vs. dE/dx_2, where 1 and 2 denote two virtual detector layers mimicking a two-element particle telescope.

Each virtual layer is defined to provide a track length of about 500 μm, corresponding to typically about 10 pixels. The present analysis therefore includes only tracks with polar angles greater than 60°, where the polar angle is defined as the angle between the detector surface normal and the particle track. It was empirically found that track lengths of 500 μm ensure good sampling of dE/dx while accepting sufficient particles to populate the plot of dE/dx_1 vs. dE/dx_2. For tracks longer than 1000 μm, the sub-clusters are created at the ends of the track and the middle part is not utilized, as shown in Fig. 1, as the evolution of dE/dx in the detector is best characterized by comparing the start and the end of the track. The angular filtering also limits the fractional error in the cluster dx calculation due to uncertainty in the depth at which a particle stops.

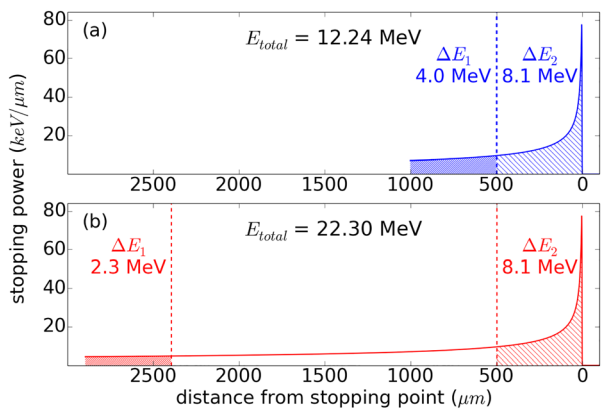

FIG. 1. Theoretical proton stopping curves in silicon for two different initial energies. The curves were calculated using the Bethe formula.[17] The regions corresponding to 500 μm at either end of the track are marked with dashed lines.

Charge-sharing effects between pixels sometimes lead to anomalously low signals at the extreme ends of a track. To account for this, following our previously described procedures,[6] we ignore the end pixels of the track when forming sub-clusters, if their energy is below a certain threshold.

We utilize data from one of the Radiation Environment Monitor (REM) units[5,16] located in the Columbus laboratory on the ISS during the period from January 1, 2014, to November 25, 2017 (more than 1200 days). The live time during this period, limited by station support computer availability, was 65%. Frames and corresponding clusters were separated into two categories corresponding to the ISS location in its orbit: South Atlantic Anomaly (SAA) and non-SAA, where galactic cosmic rays (GCR) dominate. The regions were empirically defined using detector count rates.[18] Data collected in the GCR region are the focus of the present study.

Two-dimensional histograms exhibiting dE/dx_1 vs. dE/dx_2 are shown in Fig. 2 for the GCR region. Several distinct features can be observed in these plots. Specific regions to

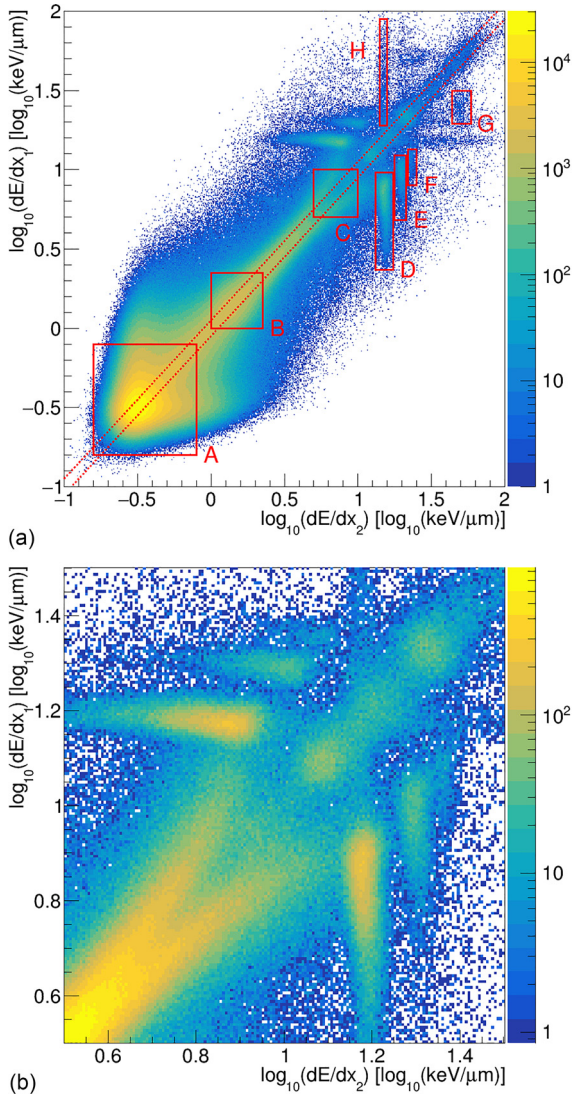

FIG. 2. Scatter plot of the dE/dx_1 vs. dE/dx_2 for data taken outside of the SAA. (a) dE/dx_1 vs. dE/dx_2 for data acquired on ISS outside of the SAA region with highlighted areas of interest. (b) Zoom of the dE/dx_1 vs. dE/dx_2 for data from (a).

be discussed are indicated in Fig. 2(a). It is notable that for penetrating particles, it is unknown which half of the cluster corresponds to the entry of the particle inside the sensor active volume. As a consequence, scatter plots show symmetry along the line defined by $dE/dx_1 = dE/dx_2$.

Area A corresponds to minimum ionizing particle (MIP) protons and other singly charged particles. The vast majority of the events in this area lie on the axis where the dE/dx for both sub-clusters is equal. Broadening about the line $dE/dx_1 = dE/dx_2$ is caused by statistical fluctuations in energy deposition for penetrating charged particles, as characterized by the Landau-Vavilov distribution.[19,20] The slice through Fig. 2(a) at $log_{10}(dE/dx) = -0.5$ (corresponding to 0.32 keV/μm) agrees well with the MIP-proton Landau-Vavilov distribution.

Area B corresponds to a mix of slower protons and MIP helium ions. At higher values of dE/dx, there is a split (Area C) where two branches diverge from the $dE/dx_1 = dE/dx_2$ line, shown in greater detail in Fig. 2(b). This part of the plot corresponds to less-energetic protons, which slow down enough in the first virtual layer to show a significant change in dE/dx.

For particles that stop inside the detector active volume, the difference between the two sub-cluster dE/dx values is substantial. These particles populate horizontal or vertical regions in a plot of dE/dx_1 vs. dE/dx_2. The appearance and location of these stripes are explained with the aid of Fig. 1, which illustrates stopping curves for protons, calculated using the Bethe formula.[17]

The particle range in the detector increases with kinetic energy, while the stopping power decreases with kinetic energy. For different particle kinetic energies, therefore, the range and the energy deposited at the beginning of the track ΔE_1 differ. The energy deposited over the last 500 μm of a stopping track, however, is independent of the particle's initial kinetic energy and varies only with the particle's charge and mass.

Integrating over the calculated curves in Fig. 1, it is found that for stopping protons, ΔE_2 is always 8.1 MeV. This value corresponds to an average dE/dx of about 16 keV/μm, the base-10 logarithm of which is 1.2. Performing similar calculations for deuterons and tritons, vertical stripes are expected at dE/dx_2 equal to 20 and 24 keV/μm, respectively ($\log_{10}(dE/dx)$ values of 1.30 and 1.38). The differences compared to protons are due to different masses and stopping powers of those isotopes. Fitting over Areas D, E, and F with Gaussian curves produces means at 15.1, 19.1, and 23.1 keV/μm, respectively, strongly supporting the association of these features with the three mentioned isotopic species, especially in view of the known bias for overestimating dx due to a lack of knowledge of the stopping depth in the sensor. For tracks long enough to result in an inferred polar angle not less than 60°, however, the resulting error in dE/dx is less than 15%. In cases where dx is over-estimated, dE/dx_2 is slightly underestimated.

Figure 1(a) presents very nearly the lowest proton energy capable of producing a track long enough to be divided into two 500 μm virtual layers. Because stopping power decreases with increasing kinetic energy (and consequently with range), ΔE_1 of 4 MeV thus represents almost the highest possible first sub-cluster energy for a proton. This corresponds to a dE/dx of 8 keV/μm, the base-10 logarithm of which is 0.9, corresponding to the highest point on the stripe in Area D. Calculating stopping curves for deuterons and tritons and applying similar analysis, it is found that the tops of the corresponding stripes are expected to be approximately 10.9 and 13.1 keV/μm, respectively [$\log_{10}(dE/dx)$ of 1.04 and 1.12]. Figure 2(b), with reference to the areas indicated in Fig. 2(a), shows that Areas D, E, and F comply closely with these predictions. Using data in these regions, the measured ratio for stopping protons to deuterons is 7.9, while for deuterons to tritons, the ratio is 4.9. Understanding these ratios has value in evaluating the accuracy of space radiation environment and transport models.

Observation of features corresponding to three hydrogen isotopes in a single layer is the result of a level of track-length resolution not possible with a single, monolithic sensor of the type used in traditional particle telescopes. In Fig. 2, dE/dx_2 is calculated using a track length corresponding to the width of 10 pixels. With a monolithic sensor, however, the track length is usually assumed to be the average path length through the sensor, resulting in large errors for some particles. Figure 3 shows the stopping-power evolution for protons stopping at different depths within a monolithic 500 μm silicon sensor, demonstrating that the integrated energy deposition in the silicon can vary considerably. Consequently, the calculated dE/dx values will exhibit significant errors, due to a lack of knowledge of the true track length.

Stopping-curve integrals for ^{3}He and ^{4}He predict ΔE_2 values of 55 and 62 keV/μm, respectively (1.74 and 1.79 in the logarithmic scale). These values agree well with Area G in Fig. 2(a). The number of clusters in this area is small, but separating ^{3}He and ^{4}He appears feasible with Timepix-based radiation detectors.

Area H represents fragmentation in the silicon sensor, producing a stopping proton. An example of such a reaction is shown in Fig. 4. Separation of these events is possible using cluster shape characteristics or morphology. To the right of Area H in Fig. 2, a fainter stripe corresponding to interactions generating a stopping deuteron can also be resolved. These events are not discernible in multi-layer telescopes since the signal from both the nuclear interaction and the stopping proton or deuteron would be summed.

dE/dx spectra measured with Timepix on ISS exhibit an artifact in the form of a spurious peak at about 12 keV/μm

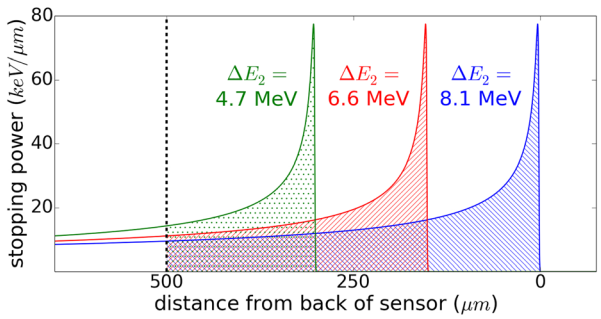

FIG. 3. Bragg curves for protons stopping at different locations within a 500 μm monolithic silicon sensor. The integral over the deposited energy in the sensor, ΔE_2, and, consequently, the calculated dE/dx depend on the depth reached by the proton before stopping.

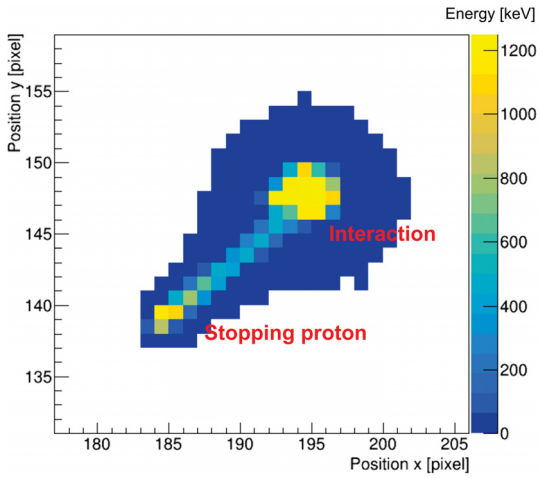

FIG. 4. An example of a nuclear interaction resulting in the stopping proton.

corresponding to miscalculation of the track length for stopping particles.[7] This artefact can be seen in the blue curve in Fig. 5, showing the whole-cluster *dE/dx* spectrum for all particles presented in Fig. 2(a). The red curve in Fig. 5 results from filtering the data such that all events outside the dashed lines in Fig. 2(a) are rejected, thus representing clusters for which *dE/dx* is relatively constant. This filtering enhances the MIP peaks of the carbon-nitrogen-oxygen ion group, with a slight indication of a boron peak. The expected locations of these features are determined using Landau-Vavilov theory[19,20] and agree well with the peaks in Fig. 5.

A single layer pixel detector can be used for identification of stopping isotopes, among other features of the space radiation environment. The ability to sample particle *dE/dx* along the trajectory, together with determining cluster morphology, makes pixel detectors an excellent tool for space radiation monitoring and environmental characterization.

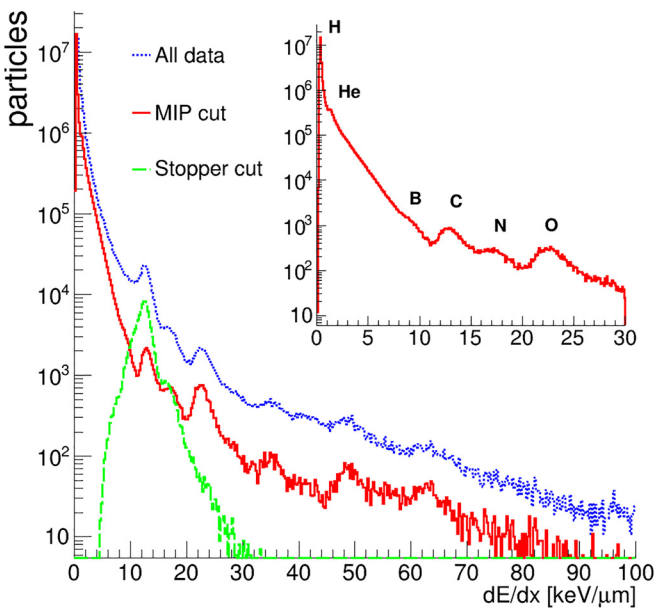

FIG. 5. *dE/dx* spectra from all data shown in Fig. 2(a) (blue), data within the dotted lines in Fig. 2(a) (red), and inferred for clusters in Areas D, E, and F (green).

A pixel-readout, single-layer telescope is shown to be capable of hydrogen isotope identification. Isotopic separation of ^{3}He and ^{4}He is feasible and could be used to help predict the source and time course of an SPE during upcoming missions outside of Earth's geomagnetic field.[21,22] Missions outside of low-Earth orbit require efficiency in all systems due to strict power and mass constraints. Systems using pixel-based space radiation detectors can meet these constraints and have been shown to provide data products that meet and exceed state-of-the-art space radiation monitoring hardware.

This work was supported by the NASA Human Health and Performance Contract (No. NNJ15HK11B) and by the Kansas State University Department of Mechanical and Nuclear Engineering and the Kansas State University Office of Engineering Research and Graduate Programs.

[1]F. A. Cucinotta, M.-H. Y. Kim, and L. J. Chappell, "Space radiation cancer risk projections and uncertainties—2012," NASA Technical Paper No. TN-2013-217375, 2012.
[2]F. A. Cucinotta, "A new approach to reduce uncertainties in space radiation cancer risk predictions," PLoS One **10**(3), e0120717 (2015).
[3]X. Llopart, R. Ballabriga, M. Campbell, L. Tlustos, and W. Wong, "Timepix, a 65k programmable pixel readout chip for arrival time, energy and/or photon counting measurements," Nucl. Instrum. Methods Phys. Res., Sect. A **581**(1–2), 485–494 (2007).
[4]N. N. Stoffle, "Viability of determining ion charge and velocity utilizing a single silicon Timepix detector," Ph.D. thesis (University of Houston, 2014).
[5]M. Kroupa, A. Bahadori, T. Campbell-Ricketts, A. Empl, S. M. Hoang, J. Idarraga-Munoz, R. Rios, E. Semones, N. Stoffle, L. Tlustos, D. Turecek, and L. Pinsky, "A semiconductor radiation imaging pixel detector for space radiation dosimetry," Life Sci. Space Res. **6**, 69–78 (2015).
[6]M. Kroupa, A. A. Bahadori, T. Campbell-Ricketts, S. P. George, and C. Zeitlin, "Kinetic energy reconstruction with a single layer particle telescope," Appl. Phys. Lett. **112**(13), 134103 (2018).
[7]N. Stoffle and L. Pinsky, "Identification of stopping ions in a silicon Timepix detector," Nucl. Instrum. Methods Phys. Res., Sect. A **880**, 35–39 (2018).
[8]A. A. Bahadori, R. P. Chowdhury, M. Kroupa, T. Campbell-Ricketts, A. Firan, D. J. Fry, R. Gaza, S. P. George, L. S. Pinsky, N. N. Stoffle, R. R. Rios, and C. J. Zeitlin, "Slowing-down and stopped charged particles cause angular dependence for absorbed dose measurements," Radiat. Phys. Chem. (in press).
[9]G. D. Badhwar, "Martian radiation environment experiment (MARIE)," in *2001 Mars Odyssey* (Springer, 2004), pp. 131–142.
[10]D. M. Hassler, C. Zeitlin, R. F. Wimmer-Schweingruber, S. Böttcher, C. Martin, J. Andrews, E. Böhm, D. E. Brinza, M. A. Bullock, S. Burmeister *et al.*, "The radiation assessment detector (RAD) investigation," Space Sci. Rev. **170**(1–4), 503–558 (2012).
[11]H. E. Spence, A. W. Case, M. J. Golightly, T. Heine, B. A. Larsen, J. B. Blake, P. Caranza, W. R. Crain, J. George, M. Lalic *et al.*, "Crater: The cosmic ray telescope for the effects of radiation experiment on the lunar reconnaissance orbiter mission," Space Sci. Rev. **150**(1–4), 243–284 (2010).
[12]L. Narici, F. Belli, V. Bidoli, M. Casolino, M. P. De Pascale, L. Di Fino, G. Furano, I. Modena, A. Morselli, P. Picozza *et al.*, "The altea/alteino projects: Studying functional effects of microgravity and cosmic radiation," Adv. Space Res. **33**(8), 1352–1357 (2004).
[13]W. B. Christie, J. L. Romero, F. P. Brady, C. E. Tull, C. M. Castaneda, E. F. Barasch, M. L. Webb, J. R. Drummond, H. J. Crawford, I. Flores, D. E. Greiner, P. J. Lindstrom, H. Sann, and J. C. Young, "A multiple sampling ionization chamber (music) for measuring the charge of relativistic heavy ions," Nucl. Instrum. Methods Phys. Res., Sect. A **255**(3), 466–476 (1987).
[14]J. Jakubek, "Precise energy calibration of pixel detector working in time-over-threshold mode," in *11th International Workshop on Radiation Imaging Detectors (IWORID)* [Nucl. Instrum. Methods Phys. Res., Sect. A **633**, S262–S266 (2011)].

[15]M. Kroupa, T. Campbell-Ricketts, A. Bahadori, and A. Empl, "Techniques for precise energy calibration of particle pixel detectors," Rev. Sci. Instrum. **88**(3), 033301 (2017).
[16]N. Stoffle, L. Pinsky, M. Kroupa, S. Hoang, J. Idarraga, C. Amberboy, R. Rios, J. Hauss, J. Keller, A. Bahadori, E. Semones, D. Turecek, J. Jakubek, Z. Vykydal, and S. Pospisil, "Timepix-based radiation environment monitor measurements aboard the International Space Station," Nucl. Instrum. Methods Phys. Res., Sect. A **782**, 143–148 (2015).
[17]H. Bethe, "Zur Theorie des Durchgangs schneller Korpuskularstrahlen durch Materie," Ann. Phys. **397**, 325–400 (1930).
[18]N. Stoffle, J. Keller, and E. Semones, "Initial report on international space station radiation environment monitor performance," NASA Technical Paper No. TM-2016-219278, 2016.
[19]P. V. Vavilov, "Ionization losses of high-energy heavy particles," Sov. Phys. JETP **5**, 749–751 (1957) [Zh. Eksp. Teor. Fiz. **32**, 920 (1957)].
[20]B. Schorr, "Programs for the Landau and the Vavilov distributions and the corresponding random numbers," Comput. Phys. Commun. **7**, 215–224 (1974).
[21]D. V. Reames, "Energetic particles from impulsive solar flares," Astrophys. J., Suppl. Ser. **73**, 235–251 (1990).
[22]D. V. Reames, "The two sources of solar energetic particles," Space Sci. Rev. **175**(1–4), 53–92 (2013).